Analytic coherent control of plasmon propagation in nanostructures

Philip Tuchscherer[1], Christian Rewitz[1], Dmitri V. Voronine[1], F. Javier García de Abajo[2], Walter Pfeiffer[3], and Tobias Brixner[1]

[1]*Institut für Physikalische Chemie, Universität Würzburg, Am Hubland, 97074 Würzburg, Germany*
[2]*Instituto de Optica, CSIC, Serrano 121, 28006 Madrid, Spain*
[3]*Fakultät für Physik, Universität Bielefeld, Universitätstr. 25, 33516 Bielefeld, Germany*
brixner@phys-chemie.uni-wuerzburg.de

Abstract: We present general analytic solutions for optical coherent control of electromagnetic energy propagation in plasmonic nanostructures. Propagating modes are excited with tightly focused ultrashort laser pulses that are shaped in amplitude, phase, and polarization (ellipticity and orientation angle). We decouple the interplay between two main mechanisms which are essential for the control of local near-fields. First, the amplitudes and the phase difference of two laser pulse polarization components are used to guide linear flux to a desired spatial position. Second, temporal compression of the near-field at the target location is achieved using the remaining free laser pulse parameter to flatten the local spectral phase. The resulting enhancement of nonlinear signals from this intuitive analytic two-step process is compared to and confirmed by the results of an iterative adaptive learning loop in which an evolutionary algorithm performs a global optimization. Thus, we gain detailed insight into why a certain complex laser pulse shape leads to a particular control target. This analytic approach may also be useful in a number of other coherent control scenarios.

OCIS codes: (320.5540) Pulse shaping, (250.5403) Plasmonics, (310.6628) Subwavelength structures

References and links

1. P. Vasa, C. Ropers, R. Pomraenke, and C. Lienau, "Ultra-fast nano-optics," Laser & Photon. Rev. (2009).
2. L. Novotny and B. Hecht, *Principles of Nano-Optics* (Cambridge University Press, 2006).
3. S. A. Maier, *Plasmonics: Fundamentals and Applications*, 1st ed. (Springer, Berlin, 2007).
4. T. Brixner, F. García de Abajo, J. Schneider, and W. Pfeiffer, "Nanoscopic Ultrafast Space-Time-Resolved Spectroscopy," Phys. Rev. Lett. **95**(9), 093,901–4 (2005).
5. S. A. Maier, M. L. Brongersma, P. G. Kik, S. Meltzer, A. A. G. Requicha, and H. A. Atwater, "Plasmonics - A Route to Nanoscale Optical Devices," Adv. Mater. **13**(19), 1501–1505 (2001).
6. S. Maier, P. Kik, H. Atwater, S. Meltzer, E. Harel, B. Koel, and A. Requicha, "Local detection of electromagnetic energy transport below the diffraction limit in metal nanoparticle plasmon waveguides," Nature Mater. **2**(4), 229–232 (2003).
7. P. Andrew and W. L. Barnes, "Energy Transfer Across a Metal Film Mediated by Surface Plasmon Polaritons," Science **306**(5698), 1002–1005 (2004).
8. W. L. Barnes, A. Dereux, and T. W. Ebbesen, "Surface plasmon subwavelength optics," Nature **424**(6950), 824–830 (2003).
9. B. Lamprecht, J. R. Krenn, G. Schider, H. Ditlbacher, M. Salerno, N. Felidj, A. Leitner, F. R. Aussenegg, and J. C. Weeber, "Surface plasmon propagation in microscale metal stripes," Appl. Phys. Lett. **79**(1), 51–53 (2001).

#111308 - $15.00 USD Received 12 May 2009; accepted 29 Jun 2009; published 31 Jul 2009

10. A. Kuzyk, M. Pettersson, J. J. Toppari, T. K. Hakala, H. Tikkanen, H. Kunttu, and P. Törmä, "Molecular coupling of light with plasmonic waveguides," Opt. Express **15**(16), 9908–9917 (2007).
11. B. Hecht, H. Bielefeldt, L. Novotny, Y. Inouye, and D. W. Pohl, "Local Excitation, Scattering, and Interference of Surface Plasmons," Phys. Rev. Lett. **77**(9), 1889 (1996).
12. P. Mühlschlegel, H. Eisler, O. J. F. Martin, B. Hecht, and D. W. Pohl, "Resonant Optical Antennas," Science **308**(5728), 1607–1609 (2005).
13. L. Novotny, "Effective Wavelength Scaling for Optical Antennas," Phys. Rev. Lett. **98**(26), 266,802–4 (2007).
14. J. Huang, T. Feichtner, P. Biagioni, and B. Hecht, "Impedance Matching and Emission Properties of Nanoantennas in an Optical Nanocircuit," Nano Lett. **9**(5), 1897–1902 (2009).
15. M. Sukharev and T. Seideman, "Phase and polarization control as a route to plasmonic nanodevices," Nano Lett. **6**(4), 715–719 (2006).
16. J. R. Krenn and J. Weeber, "Surface plasmon polaritons in metal stripes and wires," Phil. Trans. R. Soc. Lond. A **362**(1817), 739–756 (2004).
17. S. I. Bozhevolnyi, V. S. Volkov, E. Devaux, J. Laluet, and T. W. Ebbesen, "Channel plasmon subwavelength waveguide components including interferometers and ring resonators," Nature **440**(7083), 508–511 (2006).
18. J. S. Huang, D. V. Voronine, P. Tuchscherer, T. Brixner, and B. Hecht, "Deterministic spatio-temporal control of nano-optical fields in optical antennas and nano transmission lines," Phys. Rev. B **79**(19), 195,441–5 (2009).
19. M. I. Stockman, S. V. Faleev, and D. J. Bergman, "Coherent Control of Femtosecond Energy Localization in Nanosystems," Phys. Rev. Lett. **88**(6), 067,402 (2002).
20. T. Brixner, F. García de Abajo, J. Schneider, C. Spindler, and W. Pfeiffer, "Ultrafast adaptive optical near-field control," Phys. Rev. B **73**(12), 125,437–11 (2006).
21. T. Brixner, F. García de Abajo, C. Spindler, and W. Pfeiffer, "Adaptive ultrafast nano-optics in a tight focus," Appl. Phys. B **84**(1), 89–95 (2006).
22. M. Durach, A. Rusina, M. I. Stockman, and K. Nelson, "Toward Full Spatiotemporal Control on the Nanoscale," Nano Lett. **7**(10), 3145–3149 (2007).
23. X. Li and M. I. Stockman, "Highly efficient spatiotemporal coherent control in nanoplasmonics on a nanometer-femtosecond scale by time reversal," Phys. Rev. B **77**(19), 195,109–10 (2008).
24. M. Sukharev and T. Seideman, "Coherent control of light propagation via nanoparticle arrays," J. Phys. B **40**(11), S283–S298 (2007).
25. M. Aeschlimann, M. Bauer, D. Bayer, T. Brixner, F. García de Abajo, W. Pfeiffer, M. Rohmer, C. Spindler, and F. Steeb, "Adaptive subwavelength control of nano-optical fields," Nature **446**(7133), 301–304 (2007).
26. A. Kubo, K. Onda, H. Petek, Z. Sun, Y. S. Jung, and H. K. Kim, "Femtosecond Imaging of Surface Plasmon Dynamics in a Nanostructured Silver Film," Nano Lett. **5**(6), 1123–1127 (2005).
27. S. Choi, D. Park, C. Lienau, M. S. Jeong, C. C. Byeon, D. Ko, and D. S. Kim, "Femtosecond phase control of spatial localization of the optical near-field in a metal nanoslit array," Opt. Express **16**(16), 12,075–12,083 (2008).
28. M. Aeschlimann, M. Bauer, D. Bayer, T. Brixner, S. Cunovic, F. Dimler, A. Fischer, W. Pfeiffer, M. Rohmer, C. Schneider, F. Steeb, C. Strüber, and D. V. Voronine, "Simultaneous Spatial and Temporal Control of Nano-Optical Excitations," (submitted) .
29. D. J. Tannor and S. A. Rice, "Control of selectivity of chemical reaction via control of wave packet evolution," J. Chem. Phys. **83**(10), 5013–5018 (1985).
30. M. Shapiro and P. Brumer, "Laser control of product quantum state populations in unimolecular reactions," J. Chem. Phys. **84**(7), 4103–4104 (1986).
31. R. S. Judson and H. Rabitz, "Teaching lasers to control molecules," Phys. Rev. Lett. **68**(10), 1500 (1992).
32. A. Assion, T. Baumert, M. Bergt, T. Brixner, B. Kiefer, V. Seyfried, M. Strehle, and G. Gerber, "Control of Chemical Reactions by Feedback-Optimized Phase-Shaped Femtosecond Laser Pulses," Science **282**(5390), 919–922 (1998).
33. S. A. Rice and M. Zhao, *Optical Control of Molecular Dynamics*, 1st ed. (Wiley-Interscience, 2000).
34. P. W. Brumer and M. Shapiro, *Principles of the Quantum Control of Molecular Processes*, 1st ed. (Wiley & Sons, 2003).
35. A. M. Weiner, "Femtosecond pulse shaping using spatial light modulators," Rev. Sci. Instrum. **71**(5), 1929–1960 (2000).
36. T. Brixner and G. Gerber, "Femtosecond polarization pulse shaping," Opt. Lett. **26**(8), 557–559 (2001).
37. T. Brixner, G. Krampert, P. Niklaus, and G. Gerber, "Generation and characterization of polarization-shaped femtosecond laser pulses," Appl. Phys. B **74**(0), s133–s144 (2002).
38. R. Selle, P. Nuernberger, F. Langhojer, F. Dimler, S. Fechner, G. Gerber, and T. Brixner, "Generation of polarization-shaped ultraviolet femtosecond pulses," Opt. Lett. **33**(8), 803–805 (2008).
39. L. Polachek, D. Oron, and Y. Silberberg, "Full control of the spectral polarization of ultrashort pulses," Opt. Lett. **31**(5), 631–633 (2006).
40. M. Plewicki, F. Weise, S. M. Weber, and A. Lindinger, "Phase, amplitude, and polarization shaping with a pulse shaper in a Mach-Zehnder interferometer," Appl Opt **45**(32), 8354–9 (2006).
41. S. M. Weber, F. Weise, M. Plewicki, and A. Lindinger, "Interferometric generation of parametrically shaped

#111308 - $15.00 USD Received 12 May 2009; accepted 29 Jun 2009; published 31 Jul 2009

polarization pulses," Appl. Opt. **46**(23), 5987–90 (2007).
42. M. Ninck, A. Galler, T. Feurer, and T. Brixner, "Programmable common-path vector field synthesizer for femtosecond pulses," Opt. Lett. **32**(23), 3379–3381 (2007).
43. T. Baumert, T. Brixner, V. Seyfried, M. Strehle, and G. Gerber, "Femtosecond pulse shaping by an evolutionary algorithm with feedback," Appl. Phys. B **65**(6), 779–782 (1997).
44. D. Yelin, D. Meshulach, and Y. Silberberg, "Adaptive femtosecond pulse compression," Opt. Lett. **22**(23), 1793–1795 (1997).
45. P. Nuernberger, G. Vogt, T. Brixner, and G. Gerber, "Femtosecond quantum control of molecular dynamics in the condensed phase," Phys. Chem. Chem. Phys. **9**(20), 2470–97 (2007). PMID: 17508081,
46. F. García de Abajo, "Interaction of Radiation and Fast Electrons with Clusters of Dielectrics: A Multiple Scattering Approach," Phys. Rev. Lett. **82**(13), 2776 (1999).
47. E. D. Palik, *Handbook of Optical Constants of Solids* (Academic Press Inc, 1997).
48. M. Sandtke, R. J. P. Engelen, H. Schoenmaker, I. Attema, H. Dekker, I. Cerjak, J. P. Korterik, B. Segerink, and L. Kuipers, "Novel instrument for surface plasmon polariton tracking in space and time," Rev. Sci. Instrum. **79**(1), 013,704 (2008).
49. S. Mukamel, *Principles of Nonlinear Optical Spectroscopy* (Oxford University Press, USA, 1995).

1. Introduction

The emerging field of ultrafast nano-optics is a combination of femtosecond laser technology and nano-optical methods [1]. This offers unique perspectives for the confinement of light on a subwavelength spatial scale [2, 3] as well as an ultrafast time scale [4]. Propagating optical near-fields [5–10] are especially interesting for a wide range of applications, such as miniaturized photonic circuits [11], in which one would need an efficient coupling of the far-field to the near-field [2], which would then propagate and be processed by logical elements. A route to these logical processing elements are nanostructures excited with ultrashort shaped laser pulses. Plasmonic nanoantennas can be used for the efficient coupling of the laser pulses to the nanophotonic circuits [12–14]. Waveguides of nanoparticles [5,15], single stripes [8,10,16,17], and nano-transmission lines [14, 18] can be used for plasmon propagation.

In a pioneering work, Stockman *et al.* demonstrated theoretically that coherent control of nanosystems is possible with chirped laser pulses [19]. We have then reported many-parameter adaptive control of optical near-fields using polarization-shaped laser pulses [4]. Thus, it is possible to manipulate electric fields spatially and temporally on a nanometer and femtosecond scale [4, 19–23]. Sukharev *et al.* showed theoretically that with suitable elliptically polarized light one can control the propagation of electromagnetic energy in a T-junction consisting of Ag nanoparticles [15, 24]. Experimental results to tailor the optical near-field using polarization-shaped laser pulses have been demonstrated by Aeschliman *et al.* [25], and coherent pulse sequences for excitation control were employed by several groups [26, 27]. Very recently, we have achieved simultaneous control over spatial and temporal field properties experimentally [28].

Since the establishment of the phrase "coherent control" as a technical term for a research field, many controversies have emerged concerning the meaning of the word "coherent". We appreciate the relevance of the question whether some process is coherent or not. However, it appears that in many cases confusions arise because "coherent" has different meanings in different contexts and scientific communities, and that often the term is not defined precisely. For the purpose of this paper, therefore, we will use the following operational definition: Coherent control is achieved if an "output" (physical observable) depends on the spectral phase of the "input" (light field), and if a suitable phase is applied for purposes of active manipulation. This captures phase sensitivity as an essential feature for coherence. In our case, the output will be linear or non-linear flux to be defined in the sections below, and the input spectral phase is determined by the (polarization) shape of a femtosecond laser pulse.

Coherent control concepts were initially developed for and applied to molecular systems, namely chemical reaction control [29–34]. Especially the use of shaped femtosecond laser

#111308 - $15.00 USD Received 12 May 2009; accepted 29 Jun 2009; published 31 Jul 2009

pulses has been extremely successful. Femtosecond pulse shaping offers many control parameters as the spectral phase and amplitude [35] or also the polarization state [36, 37] can be modified at independent frequency positions. Further developments extended polarization shaping to the ultraviolet regime [38] and to combined amplitude and polarization control [39–41]. Recently, complete vector-field shaping with an inherently phase-stable geometry was introduced [42] now providing control over all four degrees of freedom of femtosecond light pulses independently, i.e. spectral amplitude and phase for both transverse polarization components.

In many coherent control examples, optimal control loops are employed in which a learning algorithm performs a global search for the best laser pulse shape [20, 21, 25, 31, 32, 43–45]. This has the advantage that detailed knowledge of the investigated system is not required for successful control. On the other hand, the insight into mechanisms is limited because the optimal solution is not obtained in a deterministic fashion. Hence, the question remains whether many-parameter optical control fields with complex shapes can be understood on an intuitive level such as, for example, generalized Brumer-Shapiro two-pathway interference [30].

In this work, we provide such a link and present analytic solutions to multiparameter coherent control on the example of plasmon propagation in nanostructures. We control the propagation direction in a branching waveguide structure as well as the temporal shape at the target location. The results are obtained in a deterministic fashion, thus providing the desired mechanistic insight. The outline of this work is as follows: In Section 2 we describe the basic idea, simulation details, and the definition of optimal control signals. In Section 3, we present the analytic approach to either optimize the linear flux at one location or control the direction of propagation. Polarization shaping by phase-only and with additional amplitude modulation will be treated separately. Finally, in Section 4, we present a two-step approach to control nonlinear flux in addition to the linear properties of the near-field. This also allows us to achieve analytic space-time control for a new type of spectroscopy, in which pump and probe interactions are separated both spatially and temporally. A discussion and conclusions are given in Section 5.

2. Methods

2.1. Basic idea

In a previous investigation, we have identified two main mechanisms for electromagnetic near-field control [20]. The first mechanism is a local interference of near-field modes excited by two externally applied laser pulse polarization components. Each polarization component can induce a local near-field mode that will interfere with a different local near-field mode excited by the second component. Constructive versus destructive interference can then be used to enhance or suppress the field, respectively, at certain positions in the vicinity of the nanostructure. The second control mechanism is a temporal manipulation of the local near-fields to compress the electromagnetic energy in time at a desired spatial location, thereby enhancing nonlinear signals.

In general, ultrashort laser pulses provide a large space of control parameters for guiding the plasmonic energy and focussing it on the nano-femto scale. In the present work, we make use of the full shaping capabilities, where amplitude, phase, ellipticity, and orientation angle may be arbitrarily manipulated at each frequency of the laser pulses [42]. The idea is to use an analytic approach that is based on the separation of the two control mechanisms described above. Derived spectral phases and amplitudes of each laser pulse polarization component will then be compared to adaptive optimizations. Thus, the control objective is reached in a deterministic, reproducible approach that can be understood easily.

As an example, we consider a nanostructure consisting of a branching chain of nanospheres excited with shaped laser pulses under the conditions of tight focusing (Fig. 1). The choice of this nanostructure is motivated by the experimentally observed propagation of plasmonic

#111308 - $15.00 USD Received 12 May 2009; accepted 29 Jun 2009; published 31 Jul 2009

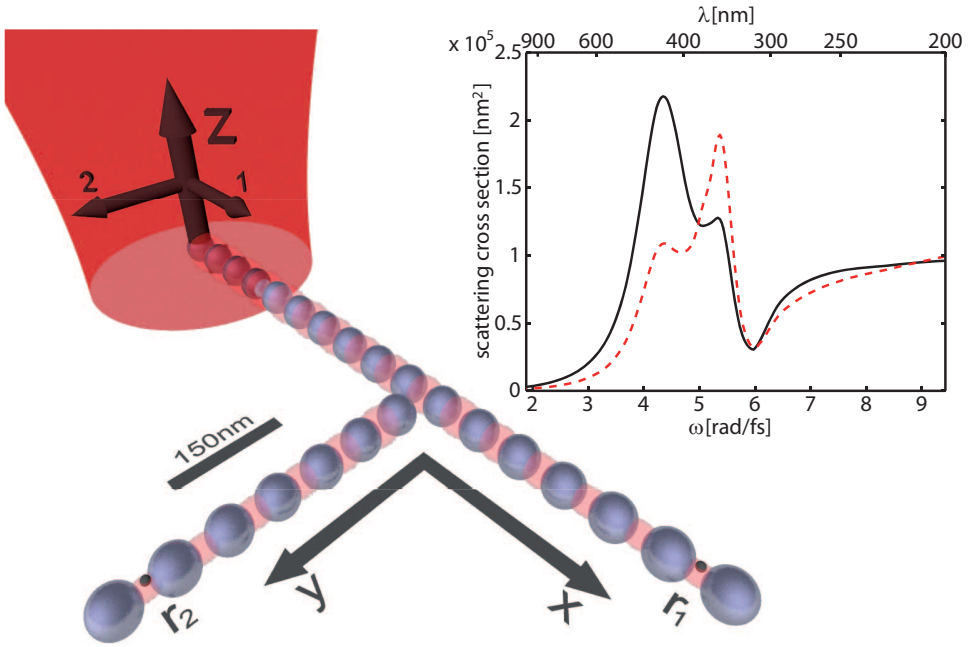

Fig. 1. Nanoplasmonic branching waveguide consisting of 50 nm diameter spheres. The target points for coherent control [$\mathbf{r}_1 = (930, 0, 10)$ nm and $\mathbf{r}_2 = (570, 380, 10)$ nm] are chosen between the last two spheres of each arm and 10 nm above the $z = 0$ symmetry plane. The structure is excited with a tightly-focused Gaussian beam (indicated in red) at the beginning of the chain using the two polarizations 1 and 2 along the x and y direction, respectively (indicated with 1 and 2 in the focus). Inset: total scattering cross sections obtained for plane wave illumination with polarization 1 (black solid) and 2 (red dashed).

excitations along such chains [6] and the recent demonstration of coherent propagation control in a T-shaped nanoparticle arrangement [15, 24]. It consists of a long chain of 17 Ag spheres along the x axis, and a short arm of seven Ag spheres along the y axis. The y arm is coupled to the long chain in the middle between the tenth and the eleventh sphere. The spheres have a diameter of 50 nm and are separated by a 10 nm gap, which corresponds to a 60 nm unit cell. The nanostructure is excited at the beginning of the long chain with a tightly-focused shaped laser pulse (focal Gaussian beam diameter of about 200 nm intensity FWHM) propagating along the z axis perpendicular to the chain with the beam center located at the center of the first sphere. Two excitation polarizations are chosen: polarization 1 along the x axis and polarization 2 along the y axis. After coupling to the nanostructure, the pulse energy is guided by plasmons away from the focus to remote spatial positions on the two branches. The inset of Fig. 1 shows the total scattering cross sections of this nanostructure excited by plane waves with polarization components 1 and 2 (black solid and red dashed curves, respectively). Clearly, two resonances are observed: the resonance of the long chain along the x direction at $\omega \sim 4.3$ rad/fs and the resonance of the short chain along the y direction at $\omega \sim 5.4$ rad/fs which are mostly excited by polarizations 1 and 2, respectively.

In a similar structure, however, with a different symmetry of the overall arrangement of the nanoparticles, Sukharev *et al.* theoretically showed the control of propagation direction after a junction by scanning the ellipticity of the excitation light using a two-dimensional parameter space [15, 24]. Here we take their work as a motivation extending it in several respects: first, we

#111308 - $15.00 USD Received 12 May 2009; accepted 29 Jun 2009; published 31 Jul 2009

introduce a multidimensional parameter space using complete vector-shaped laser pulses [42]; second, we take into account the excitation field focusing conditions; and third and most importantly, we obtain analytic control both of the linear and the nonlinear flux in nanosystems. Using this systematic approach, we decouple the interplay between the two control mechanisms described above by first guiding the linear flux to the desired point with shaping of the amplitudes of both polarization components as well as the phase difference between the two components. For linear flux the relative spectral phase is irrelevant within the pulse, since different frequency components do not interfere. For nonlinear flux, however, the different frequency components do interfere and the remaining relative spectral phase is used to enhance the nonlinear flux by compressing the local near-field at the desired point.

2.2. Field calculation

We calculate the complex-valued linear optical response of the nanostructure in the frequency domain by self-consistently solving Maxwell's equations for the given nanostructure and illumination conditions. This is done in a multiple scattering approach realized in the multiple elastic scattering of multipole expansions (MESME) code [46]. This is a fast, accurate, and general technique which can be used to obtain the linear optical response of clusters of distributed scatterers of arbitrary shapes and dimensions in the frequency domain. In the first iteration, the scattered field of individual spheres for a given incident radiation is decomposed into multipoles with respect to the center of each scattering object. In the following iteration steps, the scattered field interacts with all other scatterers and multiple scattering is carried out until convergence is achieved. Convergence in the iteration process is reinforced using the highly-convergent Lanczos method, because the direct multiple scattering expansion would lead quite often to divergence. The time required to numerically solve this problem is proportional to the square of the number of objects in the cluster. This permits one to compute radiation scattering cross sections for a cluster formed by a large number of objects within any desired degree of accuracy. As a result, we obtain the spectral field enhancement (optical response) including the phase as a function of spatial coordinates:

$$\mathbf{A}^{(i)}(\mathbf{r},\omega) = \begin{pmatrix} A_x^{(i)}(\mathbf{r},\omega) \\ A_y^{(i)}(\mathbf{r},\omega) \\ A_z^{(i)}(\mathbf{r},\omega) \end{pmatrix}. \tag{1}$$

The amplitudes $|A_\alpha^{(i)}(\mathbf{r},\omega)|$ with $\alpha = x,y,z$ describe the extent to which the two far-field polarization components $i = 1,2$ couple to the optical near-field, whereas the phases $\theta_\alpha^{(i)}(\mathbf{r},\omega) = \arg\{A_\alpha^{(i)}(\mathbf{r},\omega)\}$ determine their vectorial superposition and dispersion properties. These quantities are characteristic of the nanostructure and depend on the focussing conditions. However, the response is independent of the applied pulse shape that will be considered below.

The measured bulk dielectric function [47], including dispersion and damping effects, is incorporated in the calculations of the response. Simulations are performed for 128 equally-spaced frequencies, corresponding to 128 pixels of a common laser pulse shaper. The spectral range is chosen such that it includes the plasmonic resonance of the structure [$3.9 - 5.3$ rad/fs (corresponding to $483 - 355$ nm)]. The Gaussian laser pulse spectrum is centered in the middle of the calculated spectral range at $\omega_0 = 4.6$ rad/fs (409 nm) with a FWHM of 0.35 rad/fs corresponding to ~ 10 fs pulse duration. The field distribution in a tight focus is represented as a superposition of plane waves. For realistic simulations we use a Gaussian focus which can be achieved by a high numerical aperture. The focal spot size ($\sim$200 nm) is close to the diffraction limit, obtained by a coherent superposition of 1245 partial waves.

#111308 - $15.00 USD Received 12 May 2009; accepted 29 Jun 2009; published 31 Jul 2009

It is important to point out that plasmon excitation and propagation along the nanostructure chain is already implicitly included in $\mathbf{A}^{(i)}(\mathbf{r},\omega)$, as can be verified by inverse Fourier transformation to the time domain. In order to exemplify coherent propagation control, we will concentrate on two spatial positions, $\mathbf{r}_1$ and $\mathbf{r}_2$, as marked in Fig. 1, that are reached after plasmon propagation along the *x* arm or *y* arm, of the structure, respectively. The goal will then be to control linear and nonlinear signals at these two positions, especially contrast and pulse compression, even though the illumination region is spatially separated. In effect, this corresponds to control over direction ("spatial focusing", Section 3) and time ("temporal focusing", Section 4).

The incident laser pulse is expressed in frequency domain by two orthogonal polarization components: $E_1^{\mathrm{in}}(\omega)$, oriented along the *x* axis, and $E_2^{\mathrm{in}}(\omega)$, oriented along the *y* axis, consisting of spectral amplitudes $\sqrt{I_i(\omega)}$ and phases $\varphi_i(\omega)$ which can all be varied independently using the most recent pulse shaper technology [42]:

$$E_i^{\mathrm{in}}(\omega) = \sqrt{I_i(\omega)}\exp\left[i\varphi_i(\omega)\right]. \tag{2}$$

Due to the linearity of Maxwell's equations, the total local near-field $\mathbf{E}(\mathbf{r},\omega)$ is obtained by calculating the near-field for each far-field polarization separately and taking the linear superposition [4]:

$$\mathbf{E}(\mathbf{r},\omega) = \begin{pmatrix} A_x^{(1)}(\mathbf{r},\omega) \\ A_y^{(1)}(\mathbf{r},\omega) \\ A_z^{(1)}(\mathbf{r},\omega) \end{pmatrix} \sqrt{I_1(\omega)}\exp\left[i\varphi_1(\omega)\right] + \begin{pmatrix} A_x^{(2)}(\mathbf{r},\omega) \\ A_y^{(2)}(\mathbf{r},\omega) \\ A_z^{(2)}(\mathbf{r},\omega) \end{pmatrix} \sqrt{I_2(\omega)}\exp\left[i\varphi_2(\omega)\right]. \tag{3}$$

Since Eq. (3) gives a complete picture, i.e. the amplitude and phase of the local electric field in the frequency domain, the local electric field in the time domain $\mathbf{E}(\mathbf{r},t)$ can be obtained by inverse Fourier transforming $\mathbf{E}(\mathbf{r},\omega)$ for each vector component separately.

In Section 3 we show that the independent external far-field parameters that determine the local fields are better expressed in the following equation:

$$\mathbf{E}(\mathbf{r},\omega) = \left\{ \begin{pmatrix} A_x^{(1)}(\mathbf{r},\omega) \\ A_y^{(1)}(\mathbf{r},\omega) \\ A_z^{(1)}(\mathbf{r},\omega) \end{pmatrix} \sqrt{I_1(\omega)} + \begin{pmatrix} A_x^{(2)}(\mathbf{r},\omega) \\ A_y^{(2)}(\mathbf{r},\omega) \\ A_z^{(2)}(\mathbf{r},\omega) \end{pmatrix} \sqrt{I_2(\omega)}\exp\left[-i\Phi(\omega)\right] \right\} \times \exp\left[i\varphi_1(\omega)\right], \tag{4}$$

where the phase difference of the two external polarization components is

$$\Phi(\omega) = \varphi_1(\omega) - \varphi_2(\omega). \tag{5}$$

Below we will show that the phase difference $\Phi(\omega)$ and the spectral amplitudes $\sqrt{I_1(\omega)}$ and $\sqrt{I_2(\omega)}$ of the incident polarization components determine the local linear flux, whereas the phase offset $\varphi_1(\omega)$ provides a handle to manipulate the temporal evolution of the local fields.

2.3. Definition of signals

Using MESME and Eq. (3), we calculate the local optical near-field $\mathbf{E}(\mathbf{r},\omega)$ at any position $\mathbf{r}$ induced by a vector-field-shaped laser pulse. We then use this quantity to define different

#111308 - $15.00 USD Received 12 May 2009; accepted 29 Jun 2009; published 31 Jul 2009

signals in analogy with far-field optics: we define local spectral intensity as

$$S(\mathbf{r},\omega) = \sum_{\alpha=x,y,z} b_\alpha \left|E_\alpha(\mathbf{r},\omega)\right|^2 = \sum_{\alpha=x,y,z} b_\alpha \left|FT\left[E_\alpha(\mathbf{r},t)\right]\right|^2, \tag{6}$$

where FT indicates Fourier transformation and the parameters b_α describe which local polarization components are included in the signals. Setting $b_x = 1$ and $b_y = b_z = 0$, for example, describes field-matter interactions with transition dipoles oriented along the x axis. In the following calculations, we always use $b_x = b_y = b_z = 1$, corresponding to an isotropic distribution of dipole moments, unless mentioned otherwise. We define local linear flux

$$F_{\mathrm{lin}}(\mathbf{r}) = \int_{-\infty}^{\infty} \sum_{\alpha=x,y,z} b_\alpha E_\alpha^2(\mathbf{r},t)\, dt = \frac{1}{2\pi}\int_{\omega_{\mathrm{min}}}^{\omega_{\mathrm{max}}} S(\mathbf{r},\omega)\, d\omega \tag{7}$$

using Parseval's theorem. Assuming a Gaussian laser spectrum with a center frequency ω_0 we can neglect frequencies where the intensity is sufficiently small. Hence, we only have to integrate over an appropriate interval $\omega_{min} = \omega_0 - \Delta\omega$ to $\omega_{max} = \omega_0 + \Delta\omega$, where $\Delta\omega$ is a suitable width.

Since we consider a finite and discrete grid of frequencies (i.e. pulse-shaper pixels) separated by $\delta\omega$, the frequency integral in Eq. (7) can be replaced by a sum over all frequencies of the local spectrum defined in Eq. (6):

$$F_{\mathrm{lin}}(\mathbf{r}) = \frac{\delta\omega}{2\pi} \sum_{\omega=\omega_{\mathrm{min}}}^{\omega_{\mathrm{max}}} \sum_{\alpha=x,y,z} b_\alpha E_\alpha(\mathbf{r},\omega) E_\alpha^*(\mathbf{r},\omega), \tag{8}$$

where the star denotes complex conjugation. Below we will omit $\delta\omega/2\pi$ for simplicity as we employ the same grid for all comparisons. By inserting the definition of the optical near-field of Eq. (3) into Eq. (6), we obtain the local spectrum as a function of external laser intensities $I_i(\omega)$ and phases $\varphi_i(\omega)$:

$$\begin{aligned} S(\mathbf{r},\omega) = I_1(\omega) \sum_{\alpha=x,y,z} b_\alpha |A_\alpha^{(1)}(\mathbf{r},\omega)|^2 + I_2(\omega) \sum_{\alpha=x,y,z} b_\alpha |A_\alpha^{(2)}(\mathbf{r},\omega)|^2 \\ + 2\sqrt{I_1(\omega) I_2(\omega)}\,\mathrm{Re}\left\{A_{\mathrm{mix}}(\mathbf{r},\omega)\exp\left[i\Phi(\omega)\right]\right\}, \end{aligned} \tag{9}$$

with

$$A_{\mathrm{mix}}(\mathbf{r},\omega) = \sum_{\alpha=x,y,z} b_\alpha A_\alpha^{(1)}(\mathbf{r},\omega) A_\alpha^{(2)*}(\mathbf{r},\omega) = \left|A_{\mathrm{mix}}(\mathbf{r},\omega)\right| \exp\left[i\theta_{\mathrm{mix}}(\mathbf{r},\omega)\right], \tag{10}$$

where the phase difference $\Phi(\omega)$ is defined in Eq. (5) and Re is the real part. $A_{\mathrm{mix}}(\mathbf{r},\omega)$ is the complex scalar product with amplitude $|A_{\mathrm{mix}}(\mathbf{r},\omega)|$ and phase $\theta_{\mathrm{mix}}(\mathbf{r},\omega)$ describing the mixing of the two near-field modes $\mathbf{A}^{(1)}(\mathbf{r},\omega)$ and $\mathbf{A}^{(2)}(\mathbf{r},\omega)$, which can be calculated independently of the external field once the MESME calculation is done.

Analogously we define local nonlinear (second-order) flux as

$$F_{\mathrm{nl}}(\mathbf{r}) = \int_{-\infty}^{\infty} \left[\sum_{\alpha=x,y,z} b_\alpha E_\alpha^2(\mathbf{r},t)\right]^2 dt. \tag{11}$$

#111308 - $15.00 USD Received 12 May 2009; accepted 29 Jun 2009; published 31 Jul 2009

2.4. Adaptive Optimization

While the analytic control approach is the main topic of this work as developed in the following sections, we also carry out adaptive control with an evolutionary algorithm for comparison. The optimizations details can be found, for example, in Baumert *et al.* [43]. Briefly, for each shaping degree of freedom, i.e. $\varphi_1(\omega)$, $\varphi_2(\omega)$, $\sqrt{I_1(\omega)}$, and $\sqrt{I_2(\omega)}$, we use 32 genes to interpolate (spline interpolation) 128 parameters (pulse shaper pixels), and run the algorithm until convergence, which is usually achieved within 50 to 500 generations depending on the size of the search space. We use 40 individuals per population. 50% of the best individuals of the last generation are used to produce the new 40 individuals for the next generation, where 70% are gained from crossover, 20% from mutation and 10% from cloning. For the optimization of linear flux, we choose $F_{\mathrm{lin}}(\mathbf{r})$, and for nonlinear flux $F_{\mathrm{nl}}(\mathbf{r})$, as input for the fitness function, and contrast control is achieved by regarding flux differences between different positions as explained below. For a better identification of the lines in the figures, where the results of adaptive optimizations are compared to the analytic solutions, only every second data point of the adaptively optimized phases or amplitudes is plotted.

3. Spatial focusing of propagating near-fields

3.1. Optimization of linear flux at one position

3.1.1. Polarization shaping by phase-only modulation

The first control objective considered here is the maximization or minimization of local linear flux $F_{\mathrm{lin}}(\mathbf{r})$ at one specified location. In the examples below, this location will be chosen at either $\mathbf{r}_1$ or $\mathbf{r}_2$ as marked in Fig. 1. Equation (9) provides insight into the near-field control mechanisms. To optimize linear flux, the two laser phases $\varphi_1(\omega)$ and $\varphi_2(\omega)$ can be adjusted independently from the amplitudes $\sqrt{I_1(\omega)}$ and $\sqrt{I_2(\omega)}$ either to maximize or to minimize the last term in Eq. (9).

The amplitude of the mixed scalar product, $|A_{\mathrm{mix}}(\mathbf{r},\omega)|$, is a measure of how much the near-field modes project onto each other and determines the controllability at this point. For example, if the two near-field modes do not project onto each other, i.e. if the modes are perpendicular, they do not interfere and it is not possible to control the local linear flux with the laser pulse phases because $A_{\mathrm{mix}}(\mathbf{r},\omega) = 0$. Maximum controllability is obtained for parallel near-field modes, i.e. having a maximum projection.

The phase of the scalar product, $\theta_{\mathrm{mix}}(\mathbf{r},\omega)$, determines how the phase difference between the two external laser polarization components, $\Phi(\omega)$, should be chosen in order to make the interference term of Eq. (9) positive or negative. Constraints for the constructive [$\Phi_{\mathrm{max}}(\omega)$] and destructive [$\Phi_{\mathrm{min}}(\omega)$] interference are

$$\Phi_{\mathrm{max}}(\omega) = -\theta_{\mathrm{mix}}(\omega) \quad \text{and} \tag{12}$$

$$\Phi_{\mathrm{min}}(\omega) = -\theta_{\mathrm{mix}}(\omega) - \pi, \tag{13}$$

respectively. The dependence of linear flux on the phase difference $\Phi(\omega)$ only is due to the interference of the two near-field modes as the single control mechanism responsible for the linear signal. In other words, the local field is determined by the polarization state of the incident light and $A_{\mathrm{mix}}(\mathbf{r},\omega)$ is a measure of the controllability that can be achieved by polarization shaping (i.e. adjusting the phases of the two far-field polarization components). Setting, for example, $b_x = 1$ and $b_y = b_z = 0$ one can get a good understanding of this effect, since the phase difference $\theta_{\mathrm{mix}}(\mathbf{r},\omega) = \theta_x^{(1)}(\mathbf{r},\omega) - \theta_x^{(2)}(\mathbf{r},\omega)$ of the two near-field modes induced by the nanostructure is then just compensated exactly, leading to optimal constructive or destructive interference for given amplitudes. Including more than one component, e.g. $b_x = b_y = b_z = 1$, the sum in Eq.

#111308 - $15.00 USD Received 12 May 2009; accepted 29 Jun 2009; published 31 Jul 2009

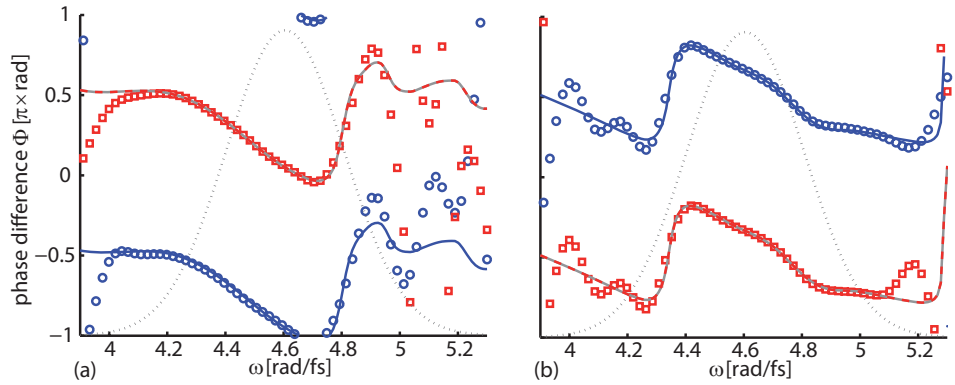

Fig. 2. The phase differences for analytic maximization (solid blue line) and minimization (dashed red line) of the linear flux $F_{\mathrm{lin}}(\mathbf{r})$ at positions $\mathbf{r}_1$ (a) and $\mathbf{r}_2$ (b) compared to the results obtained by an adaptive optimization for maximization (blue circles) and minimization (red squares). The laser spectrum is indicated by a black dotted line.

(10) performs a weighting of the phases of each component by their amplitudes. If the near-field modes are not parallel, some part of the field will still remain even for destructive interference.

The required phase difference for linear flux control is thus available directly from either Eq. (12) or Eq. (13) and is plotted in Fig. 2 for two different examples, namely the location $\mathbf{r}_1$ [Fig. 2(a)] and $\mathbf{r}_2$ [Fig. 2(b)] as solid blue lines (maximum flux) and dashed red lines (minimum flux). The plots can be understood as follows: for example, as shown in Fig. 2(a), linearly polarized light at $\omega \sim 4.65$ rad/fs oriented along the (1,1,0) direction ($\Phi = 0$) minimizes the local flux at $\mathbf{r}_1$, whereas linearly polarized light oriented along the (-1,1,0) direction ($\Phi = \pi$) maximizes the local flux at $\mathbf{r}_1$. In contrast right ($\Phi = -\pi/2$) and left ($\Phi = \pi/2$) circularly polarized light at $\omega \sim 4.25$ rad/fs generates the maximum and minimum local flux at $\mathbf{r}_1$, respectively. The control at other frequencies is achieved similarly using elliptically polarized light.

In order to confirm the analytic solutions, we performed adaptive optimizations of $F_{\mathrm{lin}}(\mathbf{r})$ using an evolutionary algorithm, and the resulting optimal spectral phases are plotted as blue circles (maximization) and red squares (minimization) in Fig. 2. Analytic and adaptive results are in excellent agreement in the region of relevant laser spectral intensity (black dotted line). The predicted difference of π between the phase differences [see Eqs. (12) and (13)] can be seen as an offset between the red and blue curves, and the shape of the curves reflects the spectral response properties of the nanostructure as contained in the scalar product of Eq. (10). Parseval's theorem guarantees that the control can be done separately for each frequency component, as shown above using analytical methods. The adaptive optimization is however performed here for the entire pulse simultaneously, and therefore the agreement with the analytic model is a non-trivial cross validation of the results.

For a better interpretation of the actual near-field responses over a broad spectral range, we define the local response intensities, i.e. the local spectrum [Eq. (9)] divided by the incident Gaussian laser spectrum $I_G(\omega)$ (see Section 3.2.2):

$$R(\mathbf{r},\omega) = \frac{S(\mathbf{r},\omega)}{I_G(\omega)}. \tag{14}$$

The local response intensities at the positions $\mathbf{r}_1$ (blue lines) and $\mathbf{r}_2$ (red lines) are shown in Fig. 3 for the optimal incident laser phase differences from Fig. 2. The maximum and minimum local linear flux phase differences are used to generate the maximum and minimum local response

#111308 - $15.00 USD Received 12 May 2009; accepted 29 Jun 2009; published 31 Jul 2009

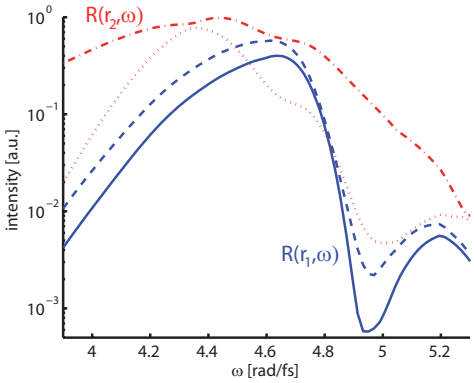

Fig. 3. The local response intensities $R(\mathbf{r},\omega)$ plotted logarithmically for the position $\mathbf{r}_1$ for the maximum (blue dashed) and minimum (blue solid) local linear flux, and for the position $\mathbf{r}_2$ (red dash-dotted and red dotted lines for the maximum and the minimum local linear flux, respectively). The optimal phase differences for the linear flux as obtained from Eq. (12) and (13) are shown in Fig. 2.

intensities, respectively. As can be seen in Fig. 3, the control of the near-fields is achieved over the whole spectral range, i.e. the blue dashed line is higher than the blue solid line, and the red dash-dotted line is higher than the red dotted line. In addition, it can be seen that the local response intensity at $\mathbf{r}_2$ (red) exceeds the local response intensity at $\mathbf{r}_1$ (blue) over a large part of the spectral range, which is due to better coupling of the two excited modes to the *y* arm. However, the minimized response at position $\mathbf{r}_2$ is smaller than the responses at position $\mathbf{r}_1$ in the region of $\omega \sim 4.7$ rad/fs, which will be relevant for the discussion of amplitude shaping in Section 3.2.2.

The linear flux values [Eq. (8)] obtained with the excitation pulse phases from Fig. 2 are summarized in Table 1 in Section 3.2.1 and will be discussed there in comparison with other control objectives.

3.1.2. Polarization shaping with additional amplitude modulation

Let us now consider polarization shaping with additional modulation of the external intensities $I_1(\omega)$ and $I_2(\omega)$, first without choosing the optimal laser pulse phases $\varphi_1(\omega)$ and $\varphi_2(\omega)$. In that case, the solutions for linear flux control at one spatial position are trivial as can be inferred from Eq. (9). Given that amplitude shaping can only decrease the intensity of light at a particular frequency, the optimal solution for maximum linear flux is full pulse-shaper transmission, i.e. making use of the full available intensity over the whole laser pulse spectrum. Likewise, the solution for minimum local flux is given for zero transmission, i.e. for both $I_i(\omega) = 0$.

However, if complete vector shaping (all phases and amplitudes) is considered, there is also a nontrivial solution for total cancellation of flux at point $\mathbf{r}$. According to Eqs. (9) and (10), the destructive interference from Section 3.1.1 can be made perfect if $\mathbf{A}^{(1)}(\mathbf{r},\omega) = \beta(\omega)\mathbf{A}^{(2)}(\mathbf{r},\omega)$, i.e. if the local responses excited by the two laser pulse polarizations are parallel to each other, with any ratio $\beta(\omega) \in \mathbb{C}$. For such a case, the external laser intensities should be chosen such that their ratio fulfills $I_1(\omega)/I_2(\omega) = |\beta(\omega)|^2$. In that case, selection of the phase difference $\Phi(\omega)$ according to Eq. (13) resulting in $\Phi(\omega) = -\arg\{\beta(\omega)\} - \pi$ leads to the desired zero flux due to perfect destructive interference. If $\mathbf{A}^{(1)}(\mathbf{r},\omega)$ and $\mathbf{A}^{(2)}(\mathbf{r},\omega)$ are not parallel, the same procedure can be used to cancel out just one component $E_\alpha(\mathbf{r},\omega)$.

#111308 - $15.00 USD Received 12 May 2009; accepted 29 Jun 2009; published 31 Jul 2009

3.2. *Controlling the direction of propagation*

With the results from Section 3.1, we can now extend the procedure to consider the more interesting case of propagation direction control. The objective will be to steer the plasmon along either the x arm or the y arm of the nanostructure (Fig. 1). In contrast to Section 3.1 the optimization goal is now determined simultaneously by the local response at two different locations, whereas in Section 3.1 both locations were treated independently. A suitable observable that characterizes this goal is the difference of linear local flux at the two spatial points $\mathbf{r}_1$ and $\mathbf{r}_2$,

$$f_{\mathrm{lin}}\left[\varphi_1(\omega),\varphi_2(\omega),I_1(\omega),I_2(\omega)\right] = F_{\mathrm{lin}}(\mathbf{r}_1) - F_{\mathrm{lin}}(\mathbf{r}_2), \tag{15}$$

which can be expressed using Eqs. (8) and (9) as

$$\begin{aligned} f_{\mathrm{lin}} &= \sum_{\omega=\omega_{\min}}^{\omega_{\max}} \sum_{\alpha=x,y,z} b_\alpha \left|E_\alpha(\mathbf{r}_1,\omega)\right|^2 - \sum_{\omega=\omega_{\min}}^{\omega_{\max}} \sum_{\alpha=x,y,z} b_\alpha \left|E_\alpha(\mathbf{r}_2,\omega)\right|^2 \\ &= \sum_{\omega=\omega_{\min}}^{\omega_{\max}} \Big(I_1(\omega)C_1(\omega) + I_2(\omega)C_2(\omega) + \\ &\qquad 2\sqrt{I_1(\omega)I_2(\omega)}\big\{ \left|A_{\mathrm{mix}}(\mathbf{r}_1,\omega)\right| \cos[\theta_{\mathrm{mix}}(\mathbf{r}_1,\omega)+\Phi(\omega)] - \\ &\qquad \left|A_{\mathrm{mix}}(\mathbf{r}_2,\omega)\right| \cos[\theta_{\mathrm{mix}}(\mathbf{r}_2,\omega)+\Phi(\omega)] \big\} \Big), \end{aligned} \tag{16}$$

where

$$C_i(\omega) = \sum_{\alpha=x,y,z} b_\alpha \left[\left|A_\alpha^{(i)}(\mathbf{r}_1,\omega)\right|^2 - \left|A_\alpha^{(i)}(\mathbf{r}_2,\omega)\right|^2 \right], \quad i=1,2, \tag{17}$$

are again functions that are determined completely by the response of the nanostructure and do not depend on the phases and amplitudes of the incident laser pulse. By finding the extrema of Eq. (16), the flux can be guided in the best possible way to either position $\mathbf{r}_1$ (f_{lin} maximum) or $\mathbf{r}_2$ (f_{lin} minimum). These extrema will be found by calculating first the correct phases (Section 3.2.1) and then the optimal amplitudes (Section 3.2.2).

3.2.1. Polarization shaping by phase-only modulation

The optimal phases can be calculated by considering the functional derivative of Eq. (16) with respect to the external phase difference,

$$\frac{\delta}{\delta\Phi(\omega)} f_{\mathrm{lin}} = \sum_{\omega=\omega_{\min}}^{\omega_{\max}} g_{\mathrm{lin}}(\omega), \tag{18}$$

with

$$\begin{aligned} g_{\mathrm{lin}}(\omega) = 2\sqrt{I_1(\omega)I_2(\omega)}\Big\{ &- \left|A_{\mathrm{mix}}(\mathbf{r}_1,\omega)\right| \sin\left[\theta_{\mathrm{mix}}(\mathbf{r}_1,\omega)+\Phi(\omega)\right] \\ &+ \left|A_{\mathrm{mix}}(\mathbf{r}_2,\omega)\right| \sin\left[\theta_{\mathrm{mix}}(\mathbf{r}_2,\omega)+\Phi(\omega)\right] \Big\}. \end{aligned} \tag{19}$$

Since we are interested in the global extremum and f_{lin} is a linear sum over the individual frequency components, each frequency can be considered separately. Thus, the extrema of f_{lin} are found for $g_{\mathrm{lin}}(\omega)=0$. Assuming $I_1(\omega)\neq 0$ and $I_2(\omega)\neq 0$ [if one or both of the intensities are zero in any frequency interval, the phases $\varphi_1(\omega)$ and $\varphi_2(\omega)$ are irrelevant for linear control

#111308 - $15.00 USD Received 12 May 2009; accepted 29 Jun 2009; published 31 Jul 2009

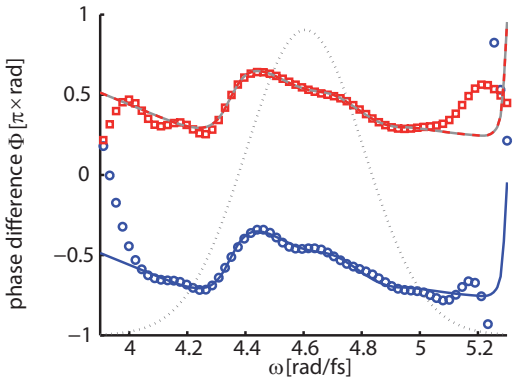

Fig. 4. Phase difference for analytic maximization (blue solid line) and minimization (red dashed line) of the linear flux difference $F_{\mathrm{lin}}(\mathbf{r}_1) - F_{\mathrm{lin}}(\mathbf{r}_2)$ and its comparison to the adaptively optimized phases (blue circles and red squares, respectively). The laser spectrum is indicated by a black dotted line.

targets and can be chosen arbitrarily], the optimal spectral phase difference is then

$$\Phi(\omega) = \arctan\left\{\frac{|A_{\mathrm{mix}}(\mathbf{r}_2,\omega)|\sin[\theta_{\mathrm{mix}}(\mathbf{r}_2,\omega)] - |A_{\mathrm{mix}}(\mathbf{r}_1,\omega)|\sin[\theta_{\mathrm{mix}}(\mathbf{r}_1,\omega)]}{|A_{\mathrm{mix}}(\mathbf{r}_1,\omega)|\cos[\theta_{\mathrm{mix}}(\mathbf{r}_1,\omega)] - |A_{\mathrm{mix}}(\mathbf{r}_2,\omega)|\cos[\theta_{\mathrm{mix}}(\mathbf{r}_2,\omega)]}\right\} + k\pi, \quad (20)$$

where $k = 0,1,2$ is chosen such that $\Phi(\omega) \in [-\pi,\pi]$. This results in two solutions that can be assigned to the global maximum or minimum by evaluation of Eq. (16) or by investigating the second derivative. For the special case of a vanishing denominator in Eq. (20), the solutions are $\Phi(\omega) = \pi/2$ and $\Phi(\omega) = -\pi/2$, which correspond to left and right circular polarization, respectively.

Just as for the optimization of linear flux at one location (Section 3.1), the flux difference of Eq. (15) depends only on the phase difference $\Phi(\omega)$ of the external polarization components and the maximum and minimum solutions differ by π. The analytically determined optimal phase difference does not depend on the pulse intensities $I_1(\omega)$ and $I_2(\omega)$. However, as we show in Section 3.2.2, shaping the amplitudes additionally results in improved contrast.

The optimal analytic phases for maximization and minimization of the linear flux difference $F_{\mathrm{lin}}(\mathbf{r}_1) - F_{\mathrm{lin}}(\mathbf{r}_2)$ for the points $\mathbf{r}_1$ and $\mathbf{r}_2$ of the chosen nanostructure are shown in Fig. 4 (lines) and are again compared to the results of an adaptive optimization (symbols). For directional control along the x arm toward $\mathbf{r}_1$ (blue) as well as along the y arm toward $\mathbf{r}_2$ (red), both approaches agree well, and the phase difference of π between maximization and minimization of the difference signal is also confirmed.

It is noticeable that the general shape depicted in Fig. 4 is similar to the shape from the optimization at point $\mathbf{r}_2$ only [Fig. 2(b)]. In this particular example, the point $\mathbf{r}_2$ has more influence on the optimal phase because the absolute value of the optimal local response intensity $R(\mathbf{r},\omega)$ is larger at $\mathbf{r}_2$ than at $\mathbf{r}_1$ over most of the spectral region (cf. Fig. 3). Therefore, the maximization (minimization) of the linear flux difference [Eq. (15)] results to a large extent from the minimization (maximization) of $F_{\mathrm{lin}}(\mathbf{r}_2)$ for the chosen nanostructure. If one chose to control flux contrast between such positions where the individual fluxes were of more similar magnitude then the optimal phase would deviate more strongly from the optimizations of both of the separate fluxes. However, with the analytic approach one has the guarantee to nevertheless find the global optimum.

#111308 - $15.00 USD Received 12 May 2009; accepted 29 Jun 2009; published 31 Jul 2009

Table 1. Analytic and adaptive linear flux control with phase-only shaping of the two polarization components. Flux values are given in the different columns for unshaped pulses corresponding to linear polarization at 45° orientation with respect to the $x-y$ coordinates and for analytic as well as adaptive flux optimization. The different rows indicate maximization and minimization of flux at the locations $\mathbf{r}_1$, $\mathbf{r}_2$, and of the flux difference. The first and the second row correspond to control at one position from Section 3.1.1 and the third row describes the contrast control from Section 3.2.1. In all cases, the Gaussian spectrum was employed without amplitude shaping. All values are normalized to the sum of the linear flux $F_{\mathrm{lin}}(\mathbf{r}_1)+F_{\mathrm{lin}}(\mathbf{r}_2)$ excited with an unshaped pulse, i.e. the first two values in the first column sum up to unity.

	$\varphi_1=\varphi_2=0$	$\varphi_1-\varphi_2=\Phi_{max}$		$\varphi_1-\varphi_2=\Phi_{min}$	
		analytic	adaptive	analytic	adaptive
$F_{\mathrm{lin}}(\mathbf{r}_1)$	0.415	0.599	0.599	0.401	0.401
$F_{\mathrm{lin}}(\mathbf{r}_2)$	0.585	0.984	0.984	0.410	0.410
$F_{\mathrm{lin}}(\mathbf{r}_1)-F_{\mathrm{lin}}(\mathbf{r}_2)$	-0.169	0.088	0.088	-0.483	-0.483

The actual flux values reached in the analytic and adaptive control strategies are summarized in Table 1. It is seen that for all cases the flux values reached in adaptive control agree extremely well with the analytic results. This points at the good convergence of the evolutionary algorithm and is another measure for the excellent agreement of the phases, already seen in Figs. 2 and 4. The difference of the linear fluxes obtained by maximizing at $\mathbf{r}_1$ and minimizing at $\mathbf{r}_2$ separately is $(0.599-0.410=0.189)$, while maximizing the difference directly leads to 0.088. The difference between minimization at $\mathbf{r}_1$ and maximization at $\mathbf{r}_2$ is $(0.401-0.984=-0.583)$, and direct contrast control yields -0.483. The optimal solution for the difference signal provides a good compromise between control at the individual points $\mathbf{r}_1$ and $\mathbf{r}_2$ for this nanostructure.

It can also be seen in Table 1 that for all control objectives the obtained maxima of the observables are higher than for unshaped pulses and the minima are lower, which is of course expected. The positive versus negative values in the bottom row indicate that "switching" of the propagation direction is achieved such that the plasmon propagates predominantly either along the x arm or the y arm of the structure. In the following section, additional amplitude shaping will even improve the control performance. It is important to point out that the results of the present section obtained for the optimal phases are valid without dependence on the particular intensities $I_1(\omega)$ and $I_2(\omega)$ of the two external polarization components. Thus the optimal amplitudes can be found in a separate step.

3.2.2. Polarization shaping with additional amplitude modulation

Amplitude shaping is described by multiplying the Gaussian input pulse amplitude $\sqrt{I_G(\omega)}$, which is the same for both polarizations i, by weighting amplitude coefficients $\gamma_i(\omega)$ varying from 0 to 1:

$$\sqrt{I_i(\omega)}=\gamma_i(\omega)\sqrt{I_G(\omega)}. \tag{21}$$

Inserting this definition into Eq. (16), we obtain a two-variable quadratic function for each frequency ω:

$$f_{\mathrm{lin}}\left[\gamma_1(\omega),\gamma_2(\omega)\right]=I_G(\omega)\left[C_1(\omega)\gamma_1^2(\omega)+C_2(\omega)\gamma_2^2(\omega)+2C_{\mathrm{mix}}(\omega)\gamma_1(\omega)\gamma_2(\omega)\right], \tag{22}$$

#111308 - $15.00 USD Received 12 May 2009; accepted 29 Jun 2009; published 31 Jul 2009

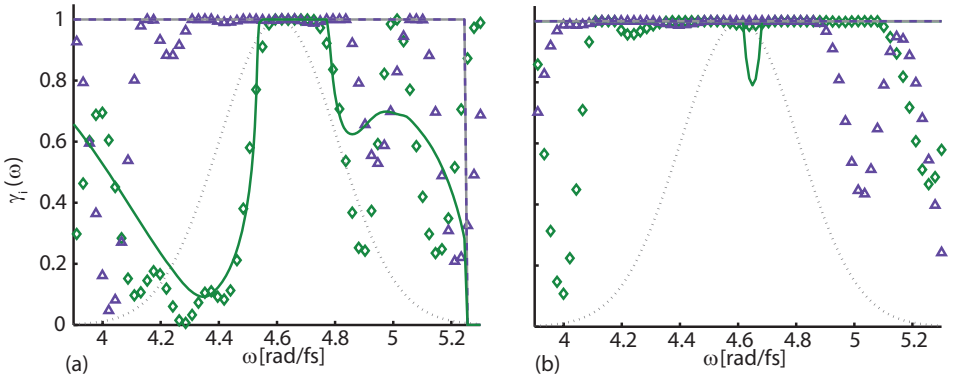

Fig. 5. Amplitude weighting coefficients for polarization components 1 (green) and 2 (purple) for controlling the linear flux difference $F_{\rm lin}(\mathbf{r}_1) - F_{\rm lin}(\mathbf{r}_2)$. The analytic results (solid and dashed lines) are compared with those from adaptive optimization (diamond and triangle symbols, respectively). The maximization or minimization of the flux difference correspond to energy guidance to positions $\mathbf{r}_1$ (a) or $\mathbf{r}_2$ (b), respectively. Pulse amplitudes are obtained by multiplying these weighting coefficients with Gaussian profiles using Eq. (21). The laser spectral intensity is indicated by a black dotted line.

where

$$C_{\rm mix}(\omega) = |A_{\rm mix}(\mathbf{r}_1,\omega)|\cos\left[\theta_{\rm mix}(\mathbf{r}_1,\omega)+\Phi(\omega)\right] - |A_{\rm mix}(\mathbf{r}_2,\omega)|\cos\left[\theta_{\rm mix}(\mathbf{r}_2,\omega)+\Phi(\omega)\right]. \tag{23}$$

Here, the parameters $|A_{\rm mix}(\mathbf{r},\omega)|$, $\theta_{\rm mix}(\mathbf{r},\omega)$, $C_i(\omega)$, and $\Phi(\omega)$ are known from Eqs. (10), (17), and (20), respectively, and the weighting amplitude coefficients for both polarization components $\gamma_1(\omega)$ and $\gamma_2(\omega)$ are unknown.

The two-variable extremum analysis of the function in Eq. (22) under the constraints $0 \leq \gamma_1(\omega) \leq 1$ and $0 \leq \gamma_2(\omega) \leq 1$ yields the solutions

$$[\gamma_1(\omega),\gamma_2(\omega)] \in \{[0,0],[1,-C_{\rm mix}(\omega)/C_2(\omega)],[-C_{\rm mix}(\omega)/C_1(\omega),1],[1,1]\}. \tag{24}$$

The assignment of which of these constitute minima or maxima depends on the values of $C_1(\omega)$, $C_2(\omega)$, and $C_{\rm mix}(\omega)$, and is found by substitution into Eq. (22). By locating the desired minimum or maximum in this fashion separately for each frequency, the optimal amplitude shape for each laser polarization component can be obtained. These solutions provide the optimal amplitudes which in turn depend on the chosen phases $\varphi_1(\omega)$ and $\varphi_2(\omega)$ through the parameter $C_{\rm mix}(\omega)$.

For illustration, we have carried out this procedure for maximization [Fig. 5(a)] as well as minimization [Fig. 5(b)] of the linear flux difference $F_{\rm lin}(\mathbf{r}_1) - F_{\rm lin}(\mathbf{r}_2)$ while using the optimal phases obtained in Section 3.2.1. Again, an evolutionary algorithm was employed for comparison, in which the phase difference as well as the amplitude weighting coefficients were optimized. In Fig. 5, analytic (lines) and adaptive results (symbols) for both polarizations are compared. Similar to Sections 3.1.1 and 3.2.1 for the case of phase shaping, the analytic and adaptive results for amplitude shaping agree well. The deviation of the amplitude coefficients from the adaptive optimizations appearing in the regions of low laser pulse intensities do not have any physical significance.

In the case of maximization [Fig. 5(a)], significant spectral shaping is required for polar-

#111308 - $15.00 USD Received 12 May 2009; accepted 29 Jun 2009; published 31 Jul 2009

ization component 1 (green) and the linear flux difference is enhanced to $F_{\mathrm{lin}}(\mathbf{r}_1) - F_{\mathrm{lin}}(\mathbf{r}_2) = 0.201$. This value should be compared to the phase-only shaping result of 0.088 (cf. Table 1). Thus, the maximum of the linear flux difference is increased significantly. However, in the case of minimization [Fig. 5(b)], the optimal amplitudes are at their maxima over most of the spectrum (both weighting coefficients equal 1). This is because amplitude shaping cannot further decrease the linear flux difference of -0.483 (cf. Table 1). For interpretation of these results, the local response intensity $R(\mathbf{r},\omega)$ shown in Fig. 3 for the two points $\mathbf{r}_1$ and $\mathbf{r}_2$ is used. The small spectral region around $\omega \sim 4.7$ rad/fs where the two responses at position $\mathbf{r}_1$ exceed the minimized response at position $\mathbf{r}_2$ is also imprinted in the weighting coefficient $\gamma_1(\omega)$ in Fig. 5(a) (green). The incident polarization component 1 is reduced in that spectral part where the local response intensity $R(\mathbf{r}_2,\omega)$ (Fig. 3) exceeds $R(\mathbf{r}_1,\omega)$. In the small part around $\omega = 4.7$ rad/fs, where $R(\mathbf{r}_1,\omega)$ dominates, both weighting coefficients equal 1 to ensure maximum contribution from the desired components.

The evolutionary algorithm confirms our predictions and successfully finds the steep slopes of amplitude coefficient $\gamma_1(\omega)$ predicted by the analytic theory.

3.3. Controlling the local spectral intensity

In addition to maximizing or minimizing the local linear flux as an integral over the whole spectrum, it is also possible to control the local spectral intensity [Eq. (6)] in a more general way, for example to maximize one part of the spectrum and simultaneously to minimize the other part. Thus, one can guide the propagation of one part of the spectrum to position $\mathbf{r}_1$ and of the other part to $\mathbf{r}_2$. For illustration, we have chosen to guide the "red" half of the spectrum ($3.9-4.6$ rad/fs) to the point $\mathbf{r}_1$, whereas the "blue" half ($4.6-5.3$ rad/fs) was guided to $\mathbf{r}_2$. The analytic results for the required optimal phases and amplitudes of the external control field are hence obtained in complete analogy to Section 3.2, only employing the results from maximization [Fig. 4 (blue) and Fig. 5(a)] in the "red" half of the spectrum and the results from minimization [Fig. 4 (red) and Fig. 5(b)] in the "blue" half. The resulting local spectrum for this control target is plotted in Fig. 6(a). The sharp peaks observed in the center of the spectrum are due to the steep slope of the amplitude coefficient $\gamma_1(\omega)$ [Fig. 5(a)] in the applied laser pulse shape, which results from the spectral part in the local response where $R(\mathbf{r}_1,\omega)$ exceeds the minimized local response $R(\mathbf{r}_2,\omega)$ shown in Fig. 3. In addition, we show the local spectrum normalized to the sum of the local spectra at positions $\mathbf{r}_1$ and $\mathbf{r}_2$ in Fig. 6(b). Note that the switching efficiency varies significantly with frequency. For some spectral components the switching efficiency is negligible (e.g., 4.5 rad/fs) whereas it is almost 100% in other regions (e.g., 4.8 rad/fs). This reflects the fact that each frequency component interferes with itself and thus the local switching efficiency is controlled by the local spectral response for each wavelength independently [20].

We successfully achieved the desired optimization goal: we were able to split the spectrum into two parts and obtain independent switching, i.e. for the lower frequencies the spectral intensity is higher at $\mathbf{r}_1$ (dashed blue) than at $\mathbf{r}_2$ (solid red), and for the higher frequencies it is higher at $\mathbf{r}_2$ than at $\mathbf{r}_1$.

4. Temporal focusing

4.1. Nonlinear flux

In Section 3 we discussed how plasmon propagation can be guided to steer local linear flux spatially. In the present section, we consider additional control of nonlinear signals. The analytic solution to temporal "focusing", i.e. the optimization of nonlinear flux, is not as straightforward as the control of linear flux. This is because the nonlinear flux defined in Eq. (11) cannot be

#111308 - $15.00 USD Received 12 May 2009; accepted 29 Jun 2009; published 31 Jul 2009

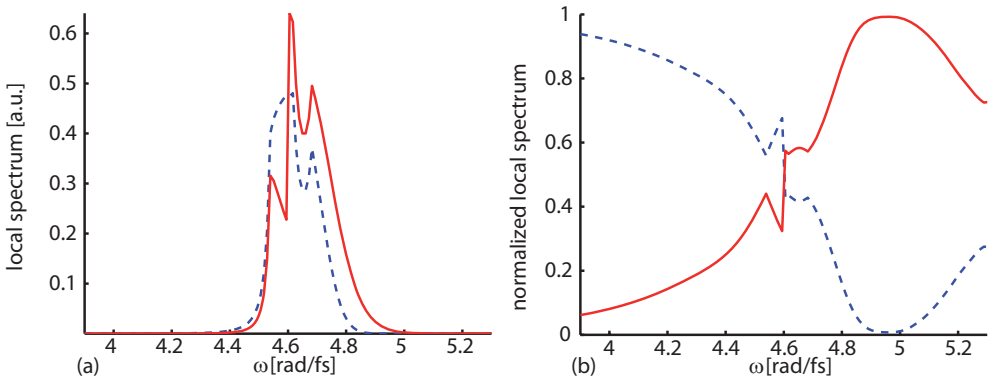

Fig. 6. (a) The local spectrum [Eq. (6)] for the optimization where the "red" and "blue" halves of the spectrum are guided to positions $\mathbf{r}_1$ (dashed blue) and $\mathbf{r}_2$ (solid red), respectively. (b) The local spectrum normalized to the sum of the local spectra at positions $\mathbf{r}_1$ and $\mathbf{r}_2$.

expressed as a linear combination of single-frequency terms in the frequency domain, as is the case for the linear quantity.

The crucial point of our approach is that in Section 3 we have obtained the optimal values for only three out of the four available degrees of freedom of the excitation laser pulse shape, and one phase can still be assigned independently, because it does not affect the linear intensity. In particular, we have used Eqs. (12), (13) or (20) to assign the phase difference $\Phi(\omega) = \varphi_1(\omega) - \varphi_2(\omega)$ between the two excitation laser polarization components, and the prescription of Section 3.1.2 or Eq. (24) to find both intensities $I_1(\omega)$ and $I_2(\omega)$. Since the linear signals depend only on the phase difference $\Phi(\omega)$, Eq. (5), which was already introduced at the beginning of this manuscript (Section 2.2), can be used to vary the phase $\varphi_1(\omega)$ under the constraint for linear flux control, i.e. given all quantities in the curly brackets. The remaining control parameter $\varphi_1(\omega)$ can then be used to control the time evolution at a certain position, in particular to compress the near-field temporally [18]. Thus, for example, we can optimize the nonlinear flux defined in Eq. (11) at that position where the linear flux was guided to.

4.1.1. One field component

We first consider the simplest case in which just one polarization component of the local field contributes to the nonlinear flux by setting $b_\alpha = 1$ and $b_\beta = b_\gamma = 0$ with $\{\alpha,\beta,\gamma\} \in \{x,y,z\}$ in Eq. (11). We choose $b_x = 1$ and $b_y = b_z = 0$ and set the control target to optimize the x component of the near-field. The issue of automated laser pulse compression in the case of conventional far-field optics has been addressed more than 10 years ago by Silberberg's group [44] and our group [43]. The basic idea is that in order to achieve the shortest possible laser pulse, a flat spectral phase is required according to the Fourier relation between frequency and time domain. In the experimental implementation, learning algorithms were used to modify the spectral phase such that a nonlinear signal (second-harmonic generation in a nonlinear crystal) was maximized. Thus the material dispersion in optical components can be compensated in order to reach highest peak intensities at the spot of the experiments.

In the context of nano-optics, we have recently discussed the same principle [18] to compensate for the phase response that is introduced by the presence of nanostructures or electromagnetic propagation through them. Hence also in the present work, we will introduce a phase by the pulse shaper such that the spectral phase of the local electric field at the target point of the

#111308 - $15.00 USD Received 12 May 2009; accepted 29 Jun 2009; published 31 Jul 2009

nanostructure is flat. In the case of only one contributing local polarization component ($b_\alpha = 1$) the required phase $\varphi_1^\alpha(\omega)$ is obtained in a straightforward manner via Eq. (5) by requiring the phase of the local field to be uniformly zero, i.e. $\arg\{E_\alpha(\mathbf{r},\omega)\} \equiv 0$. Thus, we get

$$\varphi_1^\alpha(\omega) = -\arg\left\{A_\alpha^{(1)}(\mathbf{r},\omega)\sqrt{I_1(\omega)} + A_\alpha^{(2)}(\mathbf{r},\omega)\sqrt{I_2(\omega)}\,\exp\left[-i\Phi(\omega)\right]\right\} \tag{25}$$

for a given location $\mathbf{r}$ and component α.

For illustration, we have chosen the example of directional control from Section 3.2 (with $b_x = 1$ and $b_y = b_z = 0$) as a basis and have used the parameters for maximal $f_{\mathrm{lin}} = F_{\mathrm{lin}}(\mathbf{r}_1) - F_{\mathrm{lin}}(\mathbf{r}_2)$ as constraints in Eq. (25). In addition to switching the plasmon propagation along the x arm, we request temporal compression at the target point $\mathbf{r}_1$. The resulting analytic phases and amplitudes are shown in Figs. 7(a) and 7(c) (lines), respectively, and are again compared to those found by the evolutionary algorithm (symbols). In this example, however, the fitness function for the adaptive optimization was chosen directly as the difference of the nonlinear flux at the two points $\mathbf{r}_1$ and $\mathbf{r}_2$:

$$f_{\mathrm{nl}}\left[\varphi_1(\omega), \varphi_2(\omega), \sqrt{I_1(\omega)}, \sqrt{I_2(\omega)}\right] = F_{\mathrm{nl}}(\mathbf{r}_1) - F_{\mathrm{nl}}(\mathbf{r}_2). \tag{26}$$

The agreement of the analytic phases [Fig. 7(a)] and amplitudes [Fig. 7(c)] with the ones found by the evolutionary algorithm is impressive, since we compare two different observables: for the analytic result, we have used the process of first guiding the linear flux to a desired point and then compressing the field at that position using the remaining degree of freedom, whereas with the evolutionary algorithm, the nonlinear flux is guided directly by optimizing the difference given in Eq. (26). The reason for this different choice of signals was that the direct nonlinear control is the procedure usually employed in experiments with suitable feedback signals and adaptive optimization. On the other hand, the several-step analytic procedure allows deterministic derivation of the optimal pulse shape. The agreement between lines and symbols in Figs. 7(a) and 7(c) is very good and is also reflected in the non-linear flux difference [Eq. (26)] yielding 0.0127 for the analytic and 0.0126 for the adaptive approach. This shows that our analytic approach is valid even if it does not directly model the fitness function of Eq. (26).

The same procedure can also be applied for switching the propagation along the y arm using the minimum $F_{\mathrm{lin}}(\mathbf{r}_1) - F_{\mathrm{lin}}(\mathbf{r}_2)$ from Section 3.2 (with $b_x = 1$ and $b_y = b_z = 0$) as a basis and compressing the pulse temporally at position $\mathbf{r}_2$. The optimal phases and amplitudes are compared with adaptive optimizations in Figs. 7(b) and 7(d), respectively. Here, some variations between the two approaches can be seen. However, the amplitude coefficients [Fig. 7(d)] agree reasonably well and some of the relevant features in the phases [Fig. 7(b)] are also reproduced, such as the separation between the red and the blue curves in the region above $\omega \sim 4.8$ rad/fs. Below $\omega \sim 4.6$ rad/fs, the intensities in the incident fields is reduced [Fig. 7(d)], which partly explains the deviation of the phases between the two approaches. Comparing the non-linear flux difference obtained with the analytic optimization ($-1.208\cdot10^{-9}$) to the results obtained with an adaptive optimization ($-0.377\cdot10^{-9}$) shows again the validity of our analytic approach, i.e. in this case the analytic approach performs better.

All spectral phases in Fig. 7(a) and 7(b) show a predominant negative slope with additional curvatures. This is because we have chosen as an objective the spectral near-field phase to be equal to zero for reaching pulse compression at the target location. Since the target points $\mathbf{r}_1$ and $\mathbf{r}_2$ are spatially separated from the excitation spot in our example, plasmon propagation as a function of time is relevant. The propagation time corresponds to a linear spectral phase with a positive slope such that the dominant negative slopes of Fig. 7 lead to an arrival time of $t = 0$. By adding any linear phase this timing can be modified. Only the nonlinear part of the phase is

#111308 - $15.00 USD Received 12 May 2009; accepted 29 Jun 2009; published 31 Jul 2009

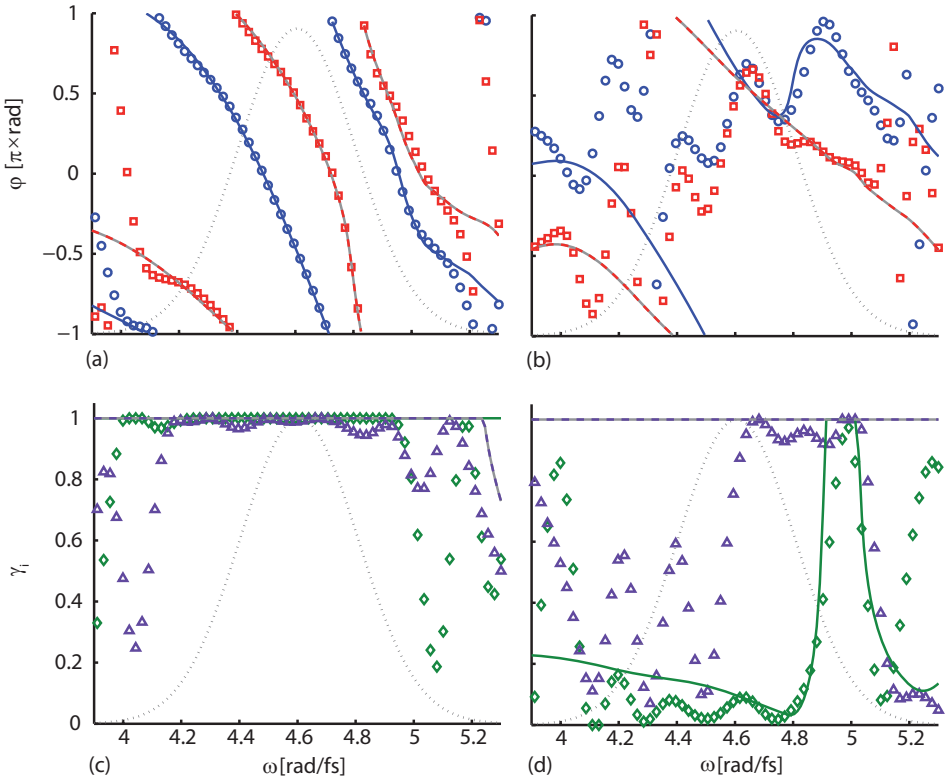

Fig. 7. Analytic (lines) phases (a,b) φ_1 (blue) and φ_2 (red) and amplitudes (c,d) $\gamma_1(\omega)$ (green) and $\gamma_2(\omega)$ (purple) for the nonlinear guidance of the *x* component of the near-field by the decoupled process of first maximizing or minimizing the linear flux difference $F_{\mathrm{lin}}(\mathbf{r}_1) - F_{\mathrm{lin}}(\mathbf{r}_2)$ and then compressing the signal at the positions $\mathbf{r}_1$ (a,c) and $\mathbf{r}_2$ (b,d), compared to the adaptively optimized (symbols) phases and amplitudes using the difference of the nonlinear signal $F_{\mathrm{nl}}(\mathbf{r}_1) - F_{\mathrm{nl}}(\mathbf{r}_2)$ [Eq. (26)] as the fitness function. The laser spectrum is indicated by a black dotted line. The adaptively optimized phases were adjusted with a linear phase and a phase offset to fit to the analytically calculated data since the evolutionary algorithm is not sensitive to these parameters.

responsible for compression.

4.1.2. Three field components

The solutions for nonlinear flux control become more complicated if we consider more than one local field component. The problem is then to assign a unique spectral phase which should in turn be compensated for pulse compression. From Eq. (5) it is clear that in general, the local spectral electric field is a three-component complex-valued vector, and each polarization component has a separate spectral phase. Thus, with $\varphi_1(\omega)$ as one (scalar) degree of freedom it is not possible to compensate for all three phases simultaneously. We therefore consider now different approximate solutions that find a suitable compromise between compensation of the different components. However, we have to divulge that due to the geometry of the chosen nanostructure, the longitudinal components, i.e. the *x* component in the *x* arm and the *y* component in the *y* arm, are dominant and are compressed in roughly the same way using both approaches.

#111308 - $15.00 USD Received 12 May 2009; accepted 29 Jun 2009; published 31 Jul 2009

First, we compensate only the phase of that component which makes the biggest contribution to the linear flux [Eq. (8)], which is found by evaluating

$$b_\alpha \sum_{\omega=\omega_{min}}^{\omega_{max}} |E_\alpha(\mathbf{r},\omega)|^2 \geq b_{\beta,\gamma} \sum_{\omega=\omega_{min}}^{\omega_{max}} \left|E_{\beta,\gamma}(\mathbf{r},\omega)\right|^2 \tag{27}$$

with $\{\alpha,\beta,\gamma\} \in \{x,y,z\}$. We then obtain the phase for component α as in Eq. (25).

In the second approach, we compensate the phase of the sum of all components weighted by their amplitude contributions to the linear signal:

$$\varphi_1^{\Sigma}(\omega) = -\arg\left\{ \sum_{\alpha=x,y,z} A_\alpha^{(1)}(\mathbf{r}_1,\omega)\sqrt{I_1(\omega)} + \sum_{\alpha=x,y,z} A_\alpha^{(2)}(\mathbf{r}_1,\omega)\sqrt{I_2(\omega)}\,\exp\left[-i\Phi(\omega)\right] \right\}. \tag{28}$$

The idea of Eq. (28) is that for maximum nonlinear flux the dominating electric-field polarization component should be compressed best.

We have carried out both approaches and again compared the analytic solutions to adaptive optimization with the fitness function of Eq. (26) [results not shown here]. In the particular structure and target positions of the example chosen here, there is not a big difference between usage of Eq. (27) and (25) or Eq. (28). But in general, nanostructures can exhibit an optical response for which comparable amplitude contributions can arise for three polarization components. Then the results will differ more strongly from either of the one-component compression results, and one of the methods from this section or a similar one can find a suitable compromise.

4.2. Interpretation of optimized fields in the time domain

The formulation of the control problem in frequency space facilitates an analytic solution as discussed in Sections 3 and 4.1. By virtue of Fourier transformation, this picture already contains all information on the temporal evolution of the different quantities. Nevertheless, it is instructive to monitor the plasmon propagation directly as a function of time, which we will do here for the analytically derived optimal excitation pulses.

Figure 8(a) shows the temporal near-field intensities reached with the excitation pulses of Section 3.2, i.e. the phase difference from Fig. 4 and amplitude coefficients from Fig. 5, combined with the phase $\varphi_1(\omega)$ for compression of the largest local near-field component [cf. (Eq. 27)], and the temporal near-fields intensities reached with an unshaped pulse. The switching of the local near-field intensity is visible by comparing the optimization of nonlinear flux guiding to $\mathbf{r}_1$ (red lines) with guiding to $\mathbf{r}_2$ (blue lines). The temporal near-fields at $\mathbf{r}_1$ and $\mathbf{r}_2$ are shown with solid and dashed-dotted lines, respectively. Clearly, the red solid line is higher than the red dashed line and the dashed blue line is higher than the solid blue line, thus confirming the successful linear flux control.

Using the nonlinear flux control we achieved both guiding of linear flux and field compression under the constraints of the amplitude-shaped spectrum. Since the effective spectral width was reduced for the linear flux control [c.f. Fig. 5(a), green curve], the bandwidth-limited pulse duration increased correspondingly. Hence, the red solid line in Fig. 8(a) has a broader width than the black solid line. The effect of dispersion compensation at $\mathbf{r}_1$ and $\mathbf{r}_2$ can be seen better in Figs. 8(b) and 8(c), respectively. Here, we compare the normalized and time-shifted temporal intensity under the constraints of guiding the linear flux, but choosing $\varphi_1(\omega) \equiv 0$ (green lines) with the normalized temporal intensity when additionally choosing the optimal $\varphi_1(\omega)$ for pulse compression (red and blue lines in Fig. 8(b) and 8(c), respectively). The compression is small in Fig. 8(b). However, for guiding to $\mathbf{r}_2$ [Fig. 8(c)] the dispersion is larger and the compression

#111308 - $15.00 USD Received 12 May 2009; accepted 29 Jun 2009; published 31 Jul 2009

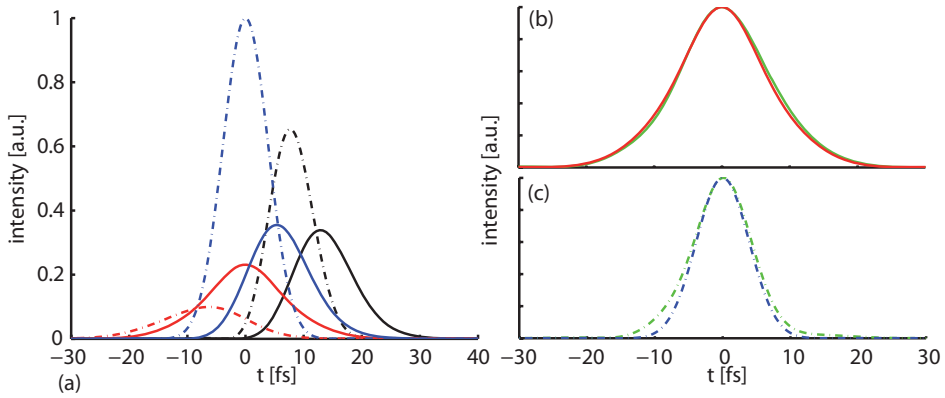

Fig. 8. (a) Temporal near-field intensity $|\mathbf{E}(\mathbf{r},t)|^2$ at two locations $\mathbf{r}_1$ (solid) and $\mathbf{r}_2$ (dashed dotted). The near-field intensity for the unshaped pulse (black) is compared to the near-field intensities excited by optimal pulses, to guide the nonlinear flux to $\mathbf{r}_1$ (red) or $\mathbf{r}_2$ (blue). (b,c) To show near-field compression the near-field intensities are plotted for the case of guiding the linear flux and choosing $\varphi_1(\omega) \equiv 0$ (green) and are compared with the near-field intensities for optimal $\varphi_1(\omega)$ for $\mathbf{r}_1$ [(b), red] and $\mathbf{r}_2$ [(c), blue]. The curves in (a) have been shifted in time and normalized for $\mathbf{r}_1$ (b) and $\mathbf{r}_2$ (c).

is more pronounced, i.e. the optimally compressed near-field (dash-dotted blue) is shorter than the near-field for pulses with $\varphi_1(\omega) \equiv 0$ (dash-dotted green).

To illustrate the spatial and temporal evolution of the propagating plasmons, we created movies that show the amplitude of the x component of the propagating near-fields excited by optimally shaped ultrashort laser pulses. Two snapshots from these movies are shown in Fig. 9, where in addition to the projections of the two laser polarization components we also show the full quasi-3D profile [36, 37] of the vector-field shaped optimal pulses.

Figure 9(a) (Media 1) shows guiding of the linear and nonlinear flux to $\mathbf{r}_1$ with the excitation phases and amplitudes of Figs. 7(a) and 7(c), respectively, and Fig. 9(b) (Media 2) shows guidance to $\mathbf{r}_2$ with the optimal field shapes from Figs. 7(b) and 7(d). Both of the snapshots are taken at $t = 0$, since the phase $\varphi_1(\omega)$ was chosen as in Eq. (25), which includes the linear spectral phase of the propagated near-field. Therefore, the excitation pulse appears at times $t < 0$ and the propagating mode arrives at the target location at $t = 0$. It can be clearly seen that after propagation from the excitation position, the field mode "switches " into the desired arm after the junction and is guided to and compressed at either $\mathbf{r}_1$ [Fig. 9(a)] or $\mathbf{r}_2$ [Fig. 9(b)].

4.3. Analytic space-time control

In previous work [4] we have suggested to use ultrafast coherent control over nano-optical fields for a new type of space-time-resolved spectroscopy below the diffraction limit. The idea was to create pump-probe-like fields in the vicinity of a nanostructure with such properties that the pump and probe interactions are not only separated in time as usual, but also occur at different spatial positions. Thus, it should be possible to develop a direct spectroscopy for transport phenomena in which the propagation of some excitation created by the pump pulse can be probed spatially and temporally at a different location. In the earlier work [4, 20], an evolutionary algorithm was used to find the optimal polarization-shaped excitation pulse. While that works for the suggested purpose, the question remained if a direct "inversion" of the problem could lead to the optimal excitation field analytically. In the present work, we use the concepts from Sections 3, 4.1, and 4.2 to provide such a prescription, and illustrate results again for the ex-

#111308 - $15.00 USD Received 12 May 2009; accepted 29 Jun 2009; published 31 Jul 2009

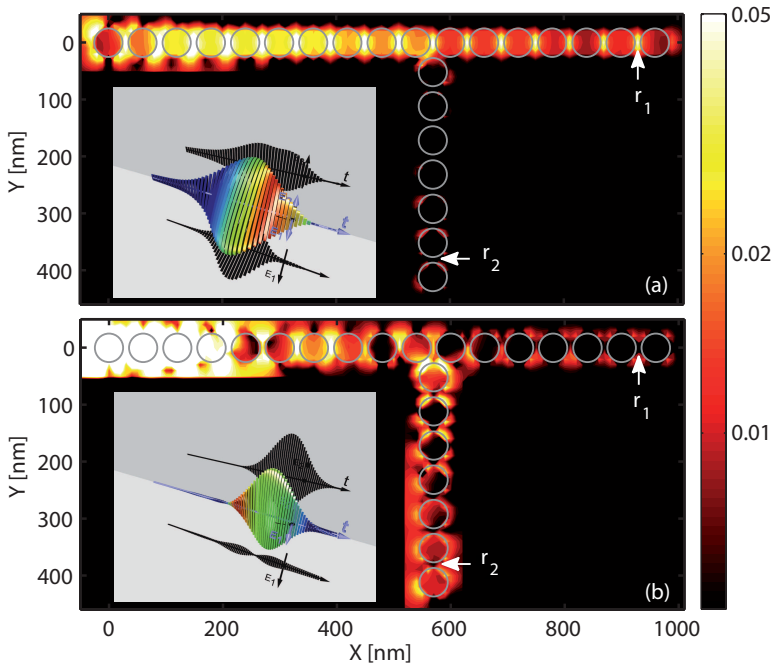

Fig. 9. Snapshots of the movies of plasmon propagation at $t = 0$ for the nonlinear flux guidance of the x component to $\mathbf{r}_1$ (a) (Media 1) and $\mathbf{r}_2$ (b) (Media 2). The amplitude of the x component of the near-field in the $z = 10$ nm plane is plotted logarithmically, where the excitation pulses are obtained by setting $b_x = 1$ and $b_y = b_z = 0$, and using the analytic approach of Sections 3.2 and 4.1. The insets show the optimal laser pulses. The arrows indicate the optimized locations.

ample of the nanostructure array of Fig. 1 and propagating plasmons. However, it should be emphasized that the method itself can be applied to arbitrary structures and does not require propagating modes.

In Section 3.1.2 we determined the optimal phase difference and amplitude coefficients to cancel out one component of the near-field at one spatial location $\mathbf{r}$. However, the near-field response at other locations is different, and therefore does not vanish. This can be used to achieve space-time control by splitting the spectrum into two parts and determining optimal pulse shapes for each of the parts independently. The temporal shape of the near-field can be optimized using the remaining free laser pulse shaping parameter $\varphi_1(\omega)$:

$$E_\alpha(\mathbf{r},\omega) = \left\{ A_\alpha^{(1)}(\mathbf{r},\omega)\sqrt{I_1(\omega)} + A_\alpha^{(2)}(\mathbf{r},\omega)\sqrt{I_2(\omega)}\exp\left[-i\Phi(\omega)\right] \right\} \exp\left[i\varphi_1(\omega)\right], \qquad (29)$$

with $\alpha = x,y,z$.

We illustrate this with one example, where the "red" half of the spectrum is used to cancel out the x component of the near-field at $\mathbf{r}_1$, while the "blue" half is used to cancel out the y component at $\mathbf{r}_2$. This gives the possibility to shape the largest local component of the signal appearing in one arm of the nanostructure independently from the signal in the other arm.

Using Eq. (25), the signal is compressed at $t = 0$, but here a time delay of $\tau = 90$ fs was introduced by requesting additional linear spectral phases with different slopes in the two spectral regions. The spectral amplitudes for the largest near-field components, i.e. the x component at $\mathbf{r}_1$ and the y component at $\mathbf{r}_2$, are plotted in Fig. 10(a). However, in Fig. 10(b) the tempo-

#111308 - $15.00 USD Received 12 May 2009; accepted 29 Jun 2009; published 31 Jul 2009

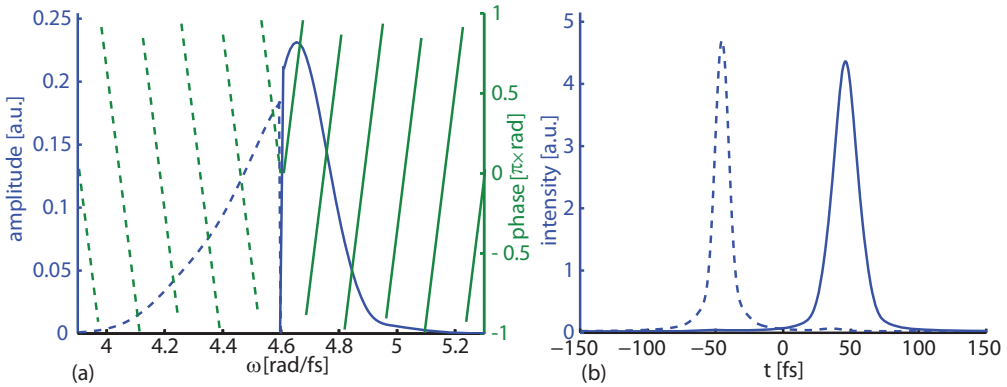

Fig. 10. (a) Spectral amplitudes (blue) and phases (green) of the largest local component of the shaped near-fields at two positions $\mathbf{r}_1$ (solid, x component) and $\mathbf{r}_2$ (dashed, y component) with the linear spectral phase corresponding to a 90 fs delay between the corresponding temporal intensities, which include all three near-field components, shown in (b).

ral intensities, which include all three components, are shown for the same polarization-shaped far-field pulse, and it can be seen that the desired spatial-temporal sequence can be reached with extremely good contrast. The pump and probe pulses peaking at $\tau = -45$ fs and $\tau = +45$ fs are limited exclusively to positions $\mathbf{r}_2$ (dashed) and $\mathbf{r}_1$ (solid), respectively.

While we have discussed a particular example here, this method is not restricted to any specific time delay or temporal shape because the two parts of the spectrum can be shaped with complete independence. Therefore, this provides an approach to perform simultaneous spatial and temporal control analytically in a very general manner.

5. Discussion and conclusions

We have derived general analytic solutions for the coherent control of nanoplasmonic energy propagation on a femtosecond time scale. In a first step, the direction of propagation at a branching point of a complex plasmonic nanostructure was controlled. Local linear flux could be switched between different target points by adjusting the interference of different near-field modes induced by the two perpendicular components of a polarization-shaped ultrashort laser pulse. Specifically, we considered the variation of all four degrees of freedom (amplitude and phase for each polarization component) that are available with recent pulse-shaping technology. The analytic results were confirmed by an evolutionary algorithm. This proves the effectiveness of the analytic approach for controlling (propagating) optical near-fields.

It is interesting that the results for controlling linear flux do not depend on the individual phases of both laser pulse polarization components but only on their difference, i.e. the polarization state. This has implications for the experimental implementation, as only the phase difference is a relevant parameter. Also, this allows us to use the remaining phase parameter for temporal control, e.g. compression for high nonlinear signals. Another interesting point is that the phases of the maximum and the minimum signals are related to each other and are different by π. Once one optimal phase is found analytically or adaptively (for example in an experiment), the other phase can be calculated immediately.

The best contrast for linear flux switching between point $\mathbf{r}_1$ and point $\mathbf{r}_2$ can be obtained if the mixed scalar products $A_{\mathrm{mix}}(\mathbf{r}_1,\omega)$ and $A_{\mathrm{mix}}(\mathbf{r}_2,\omega)$ as defined in Eq. (10) have a phase difference of $\theta_{\mathrm{mix}}(\mathbf{r}_1,\omega) - \theta_{\mathrm{mix}}(\mathbf{r}_2,\omega) = \pi$, such that the signal at $\mathbf{r}_1$ is maximized and at $\mathbf{r}_2$

#111308 - $15.00 USD Received 12 May 2009; accepted 29 Jun 2009; published 31 Jul 2009

minimized for the same phase difference $\Phi = \varphi_1 - \varphi_2$ between the two external polarization components. Considering this relation, we have also analyzed the responses of the symmetric T-structure investigated by Sukharev and Seideman [24] and observed exactly this behavior. This is the reason why the switching control in their structure works with good contrast. In general, this insight can also be used to design other nanostructures with the desired switching properties.

Apart from using the phases of the excitation laser pulse as control parameters, modifying the amplitudes as well can improve the control performance. With the analytic approach, this process can be performed separately from the phase determination. As a consequence, this insight also simplifies experiments using adaptive control because the phases and amplitudes can be determined in separate runs of the evolutionary algorithm. Thus the size of the search space is reduced dramatically, and convergence rates could improve.

Once the linear flux is guided to the desired location, the remaining phase parameter was used in an analytic approach to optimize the nonlinear flux difference. This is in principle different from the direct guiding of the nonlinear signal to the desired location. However, the results from the analytic two-step method were in good agreement with direct nonlinear guiding using the evolutionary algorithm. A complication arises if all local polarization components contribute to the nonlinear signal. In that case, it is not obvious how a function of the spectral phase should be defined, and we have discussed two different possibilities. For practical applications, the best choice depends on the precise nature of the nonlinear signal that is investigated. The definition can be adjusted to the particular system, while the general analytic approach remains the same.

In addition to spatial and temporal "focusing", it is also possible to manipulate different parts of the laser spectrum individually and independently. Thus a degree of analytic spectral control can be added to the control over spatial-temporal characteristics. As one particular example, the previously suggested [4] pump-probe pulse can now be prepared analytically such that pump and probe interactions occur not only at different times but also at different positions (with different spectral content).

The analytic scheme discussed in the present work can be used to guide the propagation of electromagnetic energy in a variety of complex nanostructures for nanoscale optical characterization, manipulation, information processing, and other applications. It is important to point out that the method is valid quite generally. We have only chosen one particular realization of a T-junction array for illustration purposes, but the analytic approach is not limited to a certain nanostructure, number of frequencies, illumination conditions, or spectral range. The only requirement is a Maxwell's equations solver which calculates the responses $\mathbf{A}^{(i)}(\mathbf{r},\omega)$ as a function of spatial position and frequency for two perpendicular incident light polarizations. It is not even necessary to calculate the response in the frequency domain, but it can also be calculated using time-domain methods, such as Finite-Difference Time Domain (FDTD), and then Fourier-transformed [18]. Similar to the theoretically obtained optical response, it should also be possible to measure it [48] for a known laser pulse and use these results for the analytic calculations of control fields.

The analytic results are not only of interest for understanding the mechanisms in optical coherent control in nanostructures, but they also present insights for how to simplify and improve experiments. Applications can be found in logical processing elements in nanophotonic circuits as well as in nonlinear spatially and temporally resolved "nano-femto" spectroscopy.

Adaptive learning loops have become a very successful technique for achieving coherent control in many different systems such as molecules or, more recently, nanostructures. However, very often the interpretation of control mechanisms is quite difficult. While in the present work we have explicitly considered a particular nanostructure and determined the optimal control of plasmon propagation analytically, we believe that the approach may be also useful for even

#111308 - $15.00 USD Received 12 May 2009; accepted 29 Jun 2009; published 31 Jul 2009

more general control scenarios, namely in molecular systems, as they can be also described in terms of optical response functions [49].

The results of this work provide a direct link between the Brumer-Shapiro frequency-space interference scheme for coherent control on the one hand [30], and many-parameter Tannor-Rice/Rabitz time-domain optimal control with shaped laser pulses on the other hand [29, 31]. The two schemes do not constitute competing approaches; we can rather combine the "best of both worlds". While it turns out that the optimal control solution such as found by a learning algorithm indeed requires a complex laser pulse shape and not just a single "control knob", that precise pulse shape can be constructed analytically by exploiting the fundamental principles of coherent two-pathway interference.

Acknowledgements

The Würzburg group gratefully acknowledges funding by the German-Israeli Foundation and the DFG (Emmy Noether Program). We thank Frank Dimler for useful discussions and help with the software. T.B. and W.P. thank the DFG within the SPP 1391.

#111308 - $15.00 USD Received 12 May 2009; accepted 29 Jun 2009; published 31 Jul 2009